MicroRNA-26b protects against MASH development in mice and can be efficiently targeted with lipid nanoparticles.

Short title: MicroRNA-26b protects against MASH

Linsey J.F. Peters[1,2,3,4,*], Leonida Rakateli[1,2,*], Rosanna Huchzermeier[1,2], Andrea Bonnin-Marquez[1,2], Sanne L. Maas[1,2], Cheng Lin[5,6], Alexander Jans[5], Yana Geng[7], Alan Gorter[7], Marion J. Gijbels[3,8], Sander S. Rensen[9], Peter Olinga[7], Tim Hendrikx[10], Marcin Krawczyk[11], Malvina Brisbois[12], Joachim Jankowski[1,2,3], Kiril Bidzhekov[4], Christian Weber[4,13,14,15,16], Erik A.L. Biessen[1,3], Ronit Shiri-Sverdlov[17], Tom Houben[17], Yvonne Döring[4,13,18], Matthias Bartneck[5,19,20], Emiel P.C. van der Vorst[1,2,4,21]

[1] Institute for Molecular Cardiovascular Research (IMCAR), RWTH Aachen University, 52056 Aachen, Germany.
[2] Aachen-Maastricht Institute for CardioRenal Disease (AMICARE), RWTH Aachen University, 52056 Aachen, Germany.
[3] Department of Pathology, Cardiovascular Research Institute Maastricht (CARIM), Maastricht University, 6229 ER Maastricht, The Netherlands.
[4] Institute for Cardiovascular Prevention (IPEK), Ludwig-Maximilians-Universität München, 80337 Munich, Germany.
[5] Department of Medicine III, University Hospital Aachen, 52074 Aachen, Germany.
[6] Department of Rheumatology and Shanghai Institute of Rheumatology, Renji
[7] Department of Pharmaceutical Technology and Biopharmacy, Groningen Research Institute of Pharmacy, University of Groningen, Groningen, The Netherlands.
[8] Department of Medical Biochemistry, Amsterdam Cardiovascular Sciences: Atherosclerosis & Ischemic Syndrome; Amsterdam Infection and Immunity: Inflammatory diseases; Amsterdam UMC location University of Amsterdam, Meibergdreef 9, Amsterdam, the Netherlands.
[9] Department of Surgery, NUTRIM, School of Nutrition and Translational Research in Metabolism, Maastricht University, 6229 ER Maastricht, Netherlands.
[10] Department of Laboratory Medicine, Medical University Vienna, Vienna, Austria.
[11] Department of Gastroenterology, Hepatology and Transplant Medicine, Medical Faculty, University of Duisburg-Essen, Essen, Germany.
[12] Department of Medicine II, Saarland University Medical Center, Saarland University, Kirrberger Str. 100, Homburg 66421, Germany
[13] DZHK (German Center for Cardiovascular Research), Partner Site Munich Heart Alliance, 80337 Munich, Germany.
[14] Department of Biochemistry, Cardiovascular Research Institute Maastricht (CARIM), Maastricht University, 6200 Maastricht, The Netherlands.
[15] Munich Cluster for Systems Neurology (SyNergy), 81377 Munich, Germany.
[16] Cluster for Nucleic Acid Therapeutics Munich (CNATM), Munich, Germany.
[17] Department of Genetics and Cell Biology, School of Nutrition and Translational Research in Metabolism (NUTRIM), University of Maastricht, Maastricht, the Netherlands.
[18] Swiss Cardiovascular Center, Division of Angiology, Inselspital, Bern University Hospital, University of Bern, CH-3010 Bern, Switzerland.
[19] DWI – Leibniz Institute for Interactive Materials, 52074 Aachen, Germany
[20] Institute of Technical and Macromolecular Chemistry, RWTH Aachen University, Germany
[21] Interdisciplinary Center for Clinical Research (IZKF), RWTH Aachen University, 52056 Aachen, Germany.
* Shared first-authorship

Grant support

This research was funded by grants from the Interdisciplinary Center for Clinical Research within the faculty of Medicine at the RWTH Aachen University, NWO-ZonMw Veni (91619053), and the Fritz Thyssen Stiftung (Grant No. 10.20.2.043MN) to E.P.C.v.d.V.; by the Austrian Science Fund (FWF) [ZK81-B, P36774-B] to T.H.; by

the DFG (BA6226/2-1, BA6226/2-3), the Wilhelm Sander Foundation (Grant No. 2018.129.1), the COST Action Mye-InfoBank 476 (CA20117), a BMBF grant (16LW0143, Mamma-Explant), the state of NRW (ZM-1-27B, NovoKolon), and an ERS grant from RWTH University (G:(DE-82)EXS-SF-OPSF732) to M.B.; by the Swiss National Foundation project ID 310030-197655 to Y.D; by a CSC stipend (ID: 202008320329) to C.L; by the 'Deutsche Forschungsgemeinschaft` (DFG, German Research Foundation) by the Transregional Collaborative Research Centre (SFB TRR219, Project-ID 322900939; and CRC 1382 (Project-ID: 403224013) to J.J; by the BMBF in the framework of the Cluster4Future program (Cluster for Nucleic Acid Therapeutics Munich, CNATM) to C.W. Human precision-cut liver slices by "Meer Kennis met Minder Dieren" under project number 114022505, which is partly financed by the ZonMw program of the Dutch Scientific Organization and Proefdiervrij to P.O.

Abbreviations

ABCA1	ATP binding cassette subfamily A member 1
ACAT2	Acetyl-CoA acetyltransferase 2
ACTA2	Actin alpha 2
BSA	Bovine serum albumin
CCL2	CC-chemokine ligand 2
CD36	Platelet glycoprotein 4
CXCL1	C-X-C motif chemokine ligand 1
eLNPs	Empty LNPs
ERK	Extracellular-signal, regulated kinase
IL-6	Interleukin-6
JNK	c-Jun-N-terminal kinase
LNP	Lipid nanoparticle
MAPK	Mitogen-activated protein kinase
MASH	Metabolic dysfunction-associated steatohepatitis
MASLD	Metabolic dysfunction-associated steatotic liver disease
mLNPs	Mimic LNPs
MMP13	Matrix metalloproteinase 13
NAFLD	Non-alcohol fatty liver disease
NF-κB	Nuclear factor-kappa B
miR-26b	MicroRNA-26b
Ox-LDL	Oxidized low-density lipoprotein
PCA	Principal component analysis
PDGFR-β	Platelet-derived growth factor receptor-beta
SEM	Standard error of the mean
Sra	Scavenger receptor a
STK	Serine/Threonine kinase
TAK1	TGF-activated kinase-1
Tgfb	transforming growth factor β
WTD	Western-type diet

Correspondence

Emiel van der Vorst
Aachen-Maastricht Institute for CardioRenal Disease (AMICARE)
Pauwelsstrasse 17, 52074, Aachen, Germany
Tel.: +49-(0)241-80-36914; Fax: +49 (0) 241 80-82716; evandervorst@ukaachen.de

Disclosures

JJ is cofounder of AMICARE GmbH. The other authors declare no conflict of interest.

Synopsis

Our study highlights the protective function of microRNA-26b in MASH by lowering lipid levels, inflammation, and fibrosis. Using microRNA-26b-containing lipid nanoparticles MASH severity was reduced in mice, providing a novel therapeutic approach that was validated in human precision-cut liver slices.

Abstract

Background & Aims. The prevalence of metabolic dysfunction-associated steatohepatitis (MASH) is increasing, urging more research into the underlying mechanisms. MicroRNA-26b (miR-26b) might play a role in several MASH-related pathways. Therefore, we aimed to determine the role of miR-26b in MASH and its therapeutic potential using miR-26b mimic-loaded lipid nanoparticles (LNPs).

Methods. *Apoe*$^{-/-}$*Mir26b*$^{-/-}$, *Apoe*$^{-/-}$*LysM*^{cre}*Mir26b*$^{fl/fl}$ mice, and respective controls were fed a western-type diet to induce MASH. Plasma and liver samples were characterized regarding lipid metabolism, hepatic inflammation, and fibrosis. Additionally, miR-26b mimic-loaded LNPs were injected in *Apoe*$^{-/-}$*Mir26b*$^{-/-}$ mice to rescue the phenotype and key results were validated in human precision-cut liver slices. Finally, kinase profiling was used to elucidate underlying mechanisms.

Results. *Apoe*$^{-/-}$*Mir26b*$^{-/-}$ mice showed increased hepatic lipid levels, coinciding with increased expression of scavenger receptor a and platelet glycoprotein 4. Similar effects were found in mice lacking myeloid-specific *miR-26b*. Additionally, hepatic TNF and IL-6 levels and amount of infiltrated macrophages were increased in *Apoe*$^{-/-}$ *Mir26b*$^{-/-}$ mice. Moreover, *Tgfb* expression was increased by the *miR-26b* deficiency, leading to more hepatic fibrosis. A murine treatment model with miR-26b mimic-loaded LNPs reduced hepatic lipids, rescuing the observed phenotype. Kinase profiling identified increased inflammatory signaling upon *miR-26b* deficiency, which was rescued by LNP treatment. Finally, miR-26b mimic-loaded LNPs also reduced inflammation in human precision-cut liver slices.

Conclusions. Overall, our study demonstrates that the detrimental effects of *miR-26b* deficiency in MASH can be rescued by LNP treatment. This novel discovery

leads to more insight into MASH development, opening doors to potential new treatment options using LNP technology.

Keywords

Metabolic dysfunction-associated steatohepatitis; hepatic inflammation; microRNAs; lipid nanoparticles

Graphical abstract

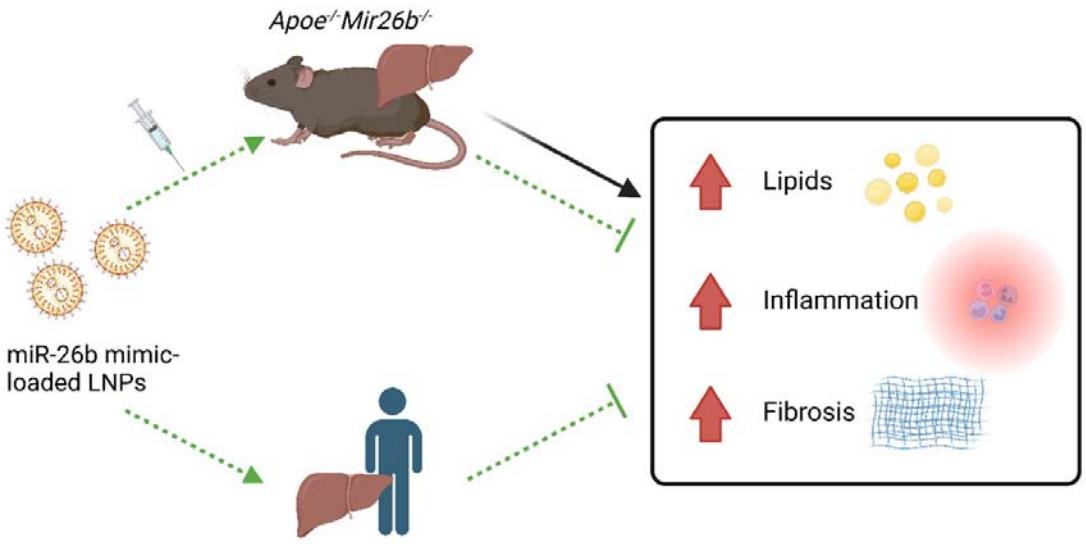

1. INTRODUCTION

‘Metabolic dysfunction-associated steatotic liver disease’ (MASLD), formerly known as non-alcohol fatty liver disease (NAFLD) [1], is the most common form of fatty liver disease. It accounts for roughly 25% of liver-disease cases globally and is defined by fat accumulation in the liver in the absence of heavy alcohol consumption [1]. MASLD refers to a group of disorders that include simple metabolic dysfunction-associated steatotic liver (MASL) and metabolic dysfunction-associated steatohepatitis (MASH) [1]. An estimated 20% to 25% of MASL patients will acquire MASH, and both MASL and MASH prevalence are predicted to rise even higher over the next decade due to increased frequency of risk factors such as obesity and insulin resistance [2]. While MASL is still considered reversible and generally benign, its progression into MASH is thought to be harmful in most cases since it precedes the development of liver fibrosis, cirrhosis, and cancer [2]. Moreover, the underlying mechanisms that initiate inflammation and cause MASL to progress into MASH are still poorly understood, which restricts the range of available treatments.

One of the main players that may be involved in these processes is microRNAs (miRs). MiRs are short non-coding RNAs that regulate gene expression post-transcriptionally by limiting messenger RNA (mRNA) translation [3]. Because miRs are involved in the control of numerous genes and processes, multiple miRs have been demonstrated to play a role in fundamental aspects of MASH, including lipid metabolism, hepatic inflammation, and fibrosis [3, 4].

Although many miRs have been examined in MASLD, the possible pathogenic involvement of numerous others, remains unknown. One of the miRs that has been researched in a number of pathologies, including cancer, cardiovascular illnesses,

and neurological disorders is miR-26b [5]. However, so far very little is known about the function of miR-26b in the liver and MASH. Nonetheless, some studies have already revealed that miR-26b may play a role in several MASH-related pathways. For example, miR-26b appears to suppress the nuclear factor-kappa B (NF-κB) pathway in human hepatocellular carcinoma cell lines by inhibiting the expression of TGF-activated kinase-1 (TAK1) and TAK1-binding protein-3, both of which are positive regulators of the NF-κB system [6]. Furthermore, miR-26b has been shown to downregulate the gene expression of platelet-derived growth factor receptor-beta (PDGFR-β), hence reducing hepatic fibrogenesis [7].

The findings above show that miR-26b may play a role in the pathogenesis of MASH, although no study has determined its exact causal involvement in MASH development. In this investigation, we used previously described miR-26b knockout mice [5] and myeloid cell-specific miR-26b knockout mice to clarify the role of miR-26b in hepatic lipid metabolism, inflammation, and fibrogenesis. Furthermore, lipid nanoparticles (LNPs), which act as clinically and therapeutically relevant vehicles [8], loaded with miR-26b mimics were used to restore miR-26b levels in mice as well as in human precision-cut liver slices to investigate its therapeutic potential.

2. METHODS

2.1 Animals

Apoe$^{-/-}$*Mir26b*$^{-/-}$ mice were generated as described in [5]. *Apoe*$^{-/-}$ mice were used as control and all mice were on C57BL/6J background for more than 10 generations. Both male and female mice were used for this study. Furthermore, myeloid lineage-specific *Mir26b*$^{fl/fl}$ mice on an *Apoe*$^{-/-}$ background were generated by crossing *Apoe*$^{-/-}$ *Mir26b*$^{fl/fl}$ (generated in house) with *Lysm*$^{Cre+}$ transgenic mice (Jackson; strain #004781) to form *Apoe*$^{-/-}$*Mir26b*$^{fl/fl}$*Lysm*$^{Cre+}$ mice. *Apoe*$^{-/-}$*Mir26b*$^{fl/fl}$*Lysm*$^{Cre-}$ mice were used as control. Starting at 8 weeks of age, the mice were fed a Western-type diet (WTD) containing 21% fat and 0.20% cholesterol (Sniff TD88137) for 4 or 12 weeks after which the mice were euthanized by intraperitoneal injection of ketamine (0.1 mg/g body weight) and xylazine (0.02 mg/g body weight). The blood was collected, and livers were harvested and snapfrozen using liquid nitrogen. The livers were embedded in Tissue-Tek O.C.T. compound (Sakura) and cryosectioned in 5µm cuts and mounted on glass slides. For metabolic measurements and further analysis, 100µm tissue sections were collected in 2ml reaction tubes. All animal studies performed were approved by the local ethical committee (Landesamt für Natur, Umwelt und Verbraucherschutz Nordrhein-Westfalen, Germany, approval number 81-02.04.2019.A363 and Regierung von Oberbayern, approval number 55.2-1-54-253245-2015).

2.2 Lipid Nanoparticle Production

The ionizable cationic lipid DLin-MC3-DMA (Hycultec GmbH, Beutelsbach, Germany) was combined with DSPC (1,2-distearoyl-sn-glycero-3-phosphorylcholine, Avanti), Cholesterol (Sigma) and DMG-PEG 2000 (Avanti) in absolute ethanol at molar ratios

of 50:10:38.5:1.5 and a final lipid concentration of 50 mM. The aqueous phase was prepared by dissolving a combination (1:1) of miRNA-26b-3P and -5P in sterile 100 mM acetate buffer (pH 4), to achieve a 0.17 µg/µL solution. For LNP formulation, the ethanol and aqueous phase were injected into a microfluidic herringbone mixer (Microfluidic ChipShop, Jena, Germany) via syringe pumps at a flow rate ratio of 1:3, respectively, with a total flow rate of 4 mL/min to obtain an N/P ratio of 4. Generated lipid nanoparticles were diluted with PBS to a concentration of ethanol below 2 %, followed by concentrating via ultra-centrifugation (3000 *xg*) using 10 kDa Amicon Ultrafilitration units (Sigma), and were finally dialyzed against PBS using a dialysis membrane with 30 kDa MWCO.

To characterize the particle size and surface charge, samples were diluted with PBS and equilibrated for 15 min at 20°C before analysis. Particle sizes and polydispersity were determined by dynamic light scattering and Zetapotential measurements were carried out both, using a Zetasizer Nano ZS (Malvern Instruments Ltd).

The encapsulation efficiency of RNA of prepared lipid nanoparticles was determined using a Quant-iT RiboGreen assay according to the instructions of the manufacturer (Thermo Fisher Scientific). Samples were analyzed by fluorescence quantification on a microplate reader (Cytation 3, BioTek Instruments Inc.). The encapsulation efficiency was calculated as the difference between the total RNA and the non-encapsulated RNA, divided by the total RNA (x100%). The dosing of RNA-LNPs was based on the Ribogreen assay result.

2.3 LNP injections

LNPs were produced as described above LNPs containing 2mg/kg RNA were administered via intraperitoneal injection every 3 days. Empty LNPs (eLNPs) and

LNPs loaded with murine miR-26b-3p (Duplex Sequences: 5'-/5Phos/rCrCrUrGrUrUrCrUrCrCrArUrUrArCrUrUrGrGmCmUrC-3' and 5'-mGmCrCmArAmGrUmArAmUrGmGrAmGrAmArCmArGG-3') and miR-26b-5p (Duplex Sequences: 5'-/5Phos/rUrUrCrArArGrUrArArUrUrCrArGrGrArUrAmGmGrU-3' and 5'-mCmUrAmUrCmCrUmGrAmArUmUrAmCrUmUrGmAA-3') mimics (IDT) were injected into *Apoe*$^{-/-}$*miRNA-26b*$^{-/-}$ mice to determine potential therapeutic effects.

2.4 RNA isolation and quantitative polymerase chain reaction

One frozen liver piece of 25mg per mouse was homogenized in a closed tube with glass beads and 1mL Qiazol by using the Tissue Lyser (Qiagen) for 5min at 50Hz. RNA was isolated using the miRNeasy mini Kit according to the manufacturer's protocol (Qiagen). Following RNA isolation, cDNA was made from 500ng total RNA by adding 1µl Oligo (dT)-Primer (Eurofins Genomics). Secondary RNA structure was denaturalized at 70˚C for 5min after which the samples were briefly cooled on ice to allow primer annealing. Subsequently, M-MLV Reverse Transcriptase, M-MLV RT 5x Buffer, and dNTP Mix (Promega) were added and cDNA synthesis was completed by incubation for 1h at 37˚C. The relative gene expression levels were determined by quantitative polymerase chain reaction (qPCR) using primer sequences listed in **Table 1**. For the qPCR reaction, 10ng of cDNA template was used to which 1X PowerUp™ SYBR™ Green Master Mix (ThermoFisher) and primers (Eurofins Genomics) were added. PCR cycling was performed on QuantStudio 3 Real-Time PCR system (ThermoFisher) with the following conditions: 50˚C for 2min for 1 cycle (UDG activation); 95˚C for 2min for 1 cycle (Dual-Lock DNA polymerase); and 95˚C

for 15sec (Denature), 58˚C for 15sec (Anneal) and 72˚C for 1min (Extend) for 40 cycles. The reference gene *Cyclophilin* was used for normalization.

Table 1. Primer sequences for genes measured with qPCR.

	Sequence in 5'-3'- direction	
Primer	**Forward**	**Reverse**
Abca1	CCCAGAGCAAAAAGCGACTC	GGTCATCATCACTTTGGTCCTTG
Acat2	ACCAATTCCAGCCATAAAGCA	GGTTTAATCCAAGTTCTTTAGCTATTGC
Acta2	ACGAACGCTTCCGCTGC	GATGCCCGCTGACTCCAT
Cd36	GCCAAGCTATTGCGACATGA	AAAAGAATCTCAATGTCCGAGACTTT
Cyclophilin	TTCCTCCTTTCACAGAATTATTCCA	CCGCCAGTGCCATTATGG
Mmp13	ACAAAGATTATCCCCGCCTCATA	CACAATGCGATTACTCCAGATACTG
Sr-A	CATACAGAAACACTGCATGTCAGAGT	TTCTGCTGATACTTTGTACACACGTT
Tgf-β	GCCCTTCCTGCTCCTCATG	CCGCACACAGCAGTTCTTCTC

For the miR-26b PCR analysis, RNA was isolated using the miRNeasy serum/plasma kit (Qiagen), according to the manufacturer's instructions. Subsequently, cDNA was generated using the TaqMan MicroRNA Reverse Transcription Kit (ThermoFisher) according to the manufacturer's instructions using 10ng of total RNA. The relative gene expression levels were determined by quantitative polymerase chain reaction (qPCR) using TaqMan MicroRNA-assays (ThermoFisher) for U6 (Assay-ID: 001973), miR-26b-3p (Assay-ID: 000407) or miR-26b-5p (Assay-ID: 002444). For the qPCR reaction, 0.5ng of cDNA template was used to which TaqMan gene expression master mix (ThermoFisher) and above-described primers were added. PCR cycling was performed on QuantStudio 3 Real-Time PCR system (ThermoFisher) with the following conditions: 50˚C for 2min for 1 cycle (UDG activation); 95˚C for 10min for 1 cycle (Dual-Lock DNA polymerase); and 95˚C for 15sec (Denature), 60˚C for 60sec (Anneal/Extend) for 40 cycles. Expression of U6 was used for normalization.

2.5 Protein isolation

One frozen liver piece of 25mg per mouse was homogenized in 0.5ml SET buffer (sucrose 250mmol/L, EDTA 2mmol/L, TRIS 10mmol/L) by vortexing briefly. Cell destruction was completed by 2 freeze-thaw cycles with liquid nitrogen and subsequently passing the sample through a 27-gauge needle for 3 times. After one last freeze-thaw cycle the total protein content was measured on the NanoDrop One Microvolume UV-Vis Spectrophotometer (ThermoFisher Scientific).

2.6 Lipid analysis

Cholesterol and triglyceride levels were quantified in liver protein lysates and EDTA-plasma using enzymatic colorimetric assays (c.f.a.s. cobas, Roche Diagnostics) according to the manufacturer's protocol. Absorbance was measured at 510nm with the microplate reader infinite M200 (Tecan).

2.7 Enzyme-linked Immunosorbent Assay

Mouse TNF, interleukin-6 (IL-6), CC-chemokine ligand 2 (CCL2), and C-X-C Motif Chemokine Ligand 1 (CXCL1) levels were measured in liver protein lysates and EDTA-plasma by enzyme-linked immunosorbent assay (ELISA) (ThermoFisher) according to the manufacturer's instructions. Absorbance was measured at 450nm with wavelength subtraction at 570nm using the microplate reader infinite M200 (Tecan).

Human TNF, IL-6, CCL2, and CXCL1 levels were measured in the supernatant of human precision-cut liver slices using ELISA (ThermoFisher) according to the manufacturer's instructions. Absorbance was measured at 450nm with wavelength subtraction at 570nm using the microplate reader infinite M200 (Tecan).

2.8 Western blotting

One 100µm liver section was lysed for 15 min on ice using M-PER Mammalian Extraction Buffer containing Halt Phosphatase Inhibitor and EDTA-free Halt Protease Inhibitor Cocktail (1:100 each; Thermo Fischer Scientific). Lysates were centrifuged for 15min at 16.000g at +4°C in a pre-cooled centrifuge. Protein quantification was performed with a NanoDrop One Microvolume UV-Vis Spectrophotometer (ThermoFisher Scientific). An equal amount of protein from each sample was resolved by 10% SDS–polyacrylamide gel electrophoresis, transferred to nitrocellulose membranes, and blocked with 5% bovine serum albumin (BSA) for 1 hour at room temperature. Anti-CD36 antibody (1:1000; Cell signalling), anti-SRA antibody (1:1000; Abcam), and anti-β-actin (1:1000; Cell signalling) were used as primary antibodies. The blots were incubated overnight at 4°C. An anti-rabbit antibody (1:1000; Cell signalling) was used and incubated for 1 hour at room

temperature. Immunoreactive bands were visualized via enhanced chemiluminescence in a ChemiDoc Imager (Bio-Rad), and densitometry was performed using Image J. β-actin was used for normalization.

2.9 Oil-red-O staining

Liver sections were prepared as described above. Following 30min drying to the air, the cryo sections were fixed with 3.5% formaldehyde for 30min at room temperature. Then the liver sections were stained with Oil-red-O (Sigma-Aldrich) for 1 hour and counterstained with Mayer's heamlum solution (Merck) for 30sec. After mounting the slides with glycerin jelly, images were acquired with an automated upright microscope (Leica microsystems), and the lipid content in the livers was quantified using ImageJ Fiji software (Laboratory for Optical and Computational Instrumentation, University of Wisconsin-Madison, Madison, Wisconsin, United States). All analyses were performed in a blinded manner.

2.10 Immunofluorescent stainings

For the visualization of inflammation and leukocyte infiltration, several immunofluorescent stainings were performed. The cryo-sectioned livers were first air-dried for 5min at room temperature and subsequently fixed with ice-cold acetone for 10min. Tissue sections were blocked with 1% bovine serum albumin (BSA) and 0.03% normal horse serum blocking solution (Vector) in 1X PBS for 1h. Neutrophils, resident macrophages, infiltrating neutrophils and macrophages, and T-cells were visualized by staining with anti-mouse Ly6G (Biolegend, dilution 1:100), anti-mouse CD68 (Biolegend, dilution 1:250), anti-mouse Mac-1 (R&D Systems, dilution 1:100) or anti-mouse CD3 (Abcam, dilution 1:100), respectively, overnight at 4˚C. Liver

sections were incubated with secondary antibodies Cy3-conjugated donkey anti-rat IgG (Jackson ImmunoResearch, dilution 1:300) or Cy3-conjugated donkey anti-rabbit IgG (Jackson ImmunoResearch, dilution 1:300) for 30min at room temperature after which nuclei were stained with Hoechst (ThermoFisher, dilution 1:10,000) for 10min at room temperature. Following the staining, the sections were mounted with Immuno-Mount (ThermoFisher), and images were acquired using an inverted microscope Dmi8 (Leica microsystems). The number of Ly6-G, CD68, Mac-1, and CD3 positive immune cells was counted with the ImageJ Fiji software. All analyses were performed in a blinded manner.

2.11 Picrosirius red staining

Liver fibrosis was visualized by a Picrosirius red staining. First, the liver sections were fixed for 2h in 10% formalin. This was followed by a 90min incubation with 0,1% Sirius Red (Polysciences) in 1% saturated picric acid solution (Applichem). Slides were subsequently incubated in 0.01N HCl for 2min and dehydrated using an ethanol range. After incubation in xylol, the slides were mounted with Vitro-Clud (R.Langenbrinck). Images were acquired using an automated upright microscope (Leica microsystems), after which the sirius red positive area was analyzed and calculated in each liver section by using ImageJ Fiji. All analyses were performed in a blinded manner.

2.12 Kinase activity profiling

Serine-Threonine kinase profiles were determined using the PamChip® Ser/Thr Kinase assay (STK; PamGene International, ´s-Hertogenbosch, The Netherlands). Each STK-PamChip® array contains 144 individual phospho-site(s) that are peptide sequences derived from substrates for Ser/Thr kinases. One 100µm liver section was

lysed for 15 min on ice using M-PER Mammalian Extraction Buffer containing Halt Phosphatase Inhibitor and EDTA-free Halt Protease Inhibitor Cocktail (1:100 each; Thermo Fischer Scientific). Lysates were centrifuged for 15min at 16.000g at +4°C in a pre-cooled centrifuge. Protein quantification was performed with a NanoDrop One Microvolume UV-Vis Spectrophotometer (ThermoFisher Scientific).

For the STK assay, 2.0µg of protein and 400µM ATP were applied per array (n=4 per condition) together with an antibody mix to detect the phosphorylated Ser/Thr. After incubation for an hour (30°C) where the sample is pumped back and forth through the porous material to maximize binding kinetics and minimize assay time, a 2nd FITC-conjugated antibody is used to detect the phosphorylation signal. Imaging was done using an LED imaging system and the spot intensity at each time point was quantified (and corrected for local background) using the BioNavigator software version 6.3 (PamGene International, 's-Hertogenbosch, The Netherlands). Upstream Kinase Analysis (UKA), a functional scoring method (PamGene) was used to rank kinases based on combined specificity scores (based on peptides linked to a kinase, derived

from 6 databases) and sensitivity scores (based on treatment-control differences).

For the peptides, a principal component analysis (PCA) was performed with the help of the R package stats V4.3.1 depicting the singular peptide decomposition examining the covariances / correlations between the samples. The R package gglot2 v3.4.2 was used to visualize the results. The distribution of the phosphorylated peptides is shown in the volcano plots created with the R package EnhancedVolcano v1.18.0. Blue dots depict peptides with an adjusted P value <0.05.

For kinases, the median final score of the kinase with a score > 1.2 and with an adjusted P value for multiple comparisons by the false discovery rate (FDR) of <0.05

are depicted in a heatmap. The R package disease ontology semantic and enrichment analysis (DOSE) [9] was utilized to analyze the enriched pathways depicting the biological complexities in which these kinases correlate with multiple annotation categories, which was visualized in a network plot with the help of the R package Reactome Pathway Analysis (ReactomePA) v1.44.0 [10].

2.13 Precision-cut liver slices

Small human liver wedges of an equivalent size of approximately 10g were collected from 3 human donors following partial resection or when livers were unsuitable for transplantation. The study was approved by the Medical Ethical Committee of the University Medical Centre Groningen (UMCG), according to Dutch legislation and the Code of Conduct for dealing responsibly with human tissue in the context of health research, refraining the need for written consent for 'further use' of coded-anonymous human tissue. The procedures were carried out in accordance with the experimental protocols approved by the Medical Ethical Committee of the UMCG. Liver tissue was stored in University of Wisconsin preservation solution (UW, 4°C). The total cold ischemic time was between 3 and 29h. Slice viability for each donor liver was tested after one hour of culture by checking ATP production as previously described [11]. Slices were cultured in GFIPO medium [12] (36mM Glucose, 5mM Fructose, 1nM Insulin, 480 µM Oleic acid, 240µM Palmitic acid) and cultured for 24 h and 48 h in the presence of empty LNPs (eLNPs) or LNPs loaded with murine miR-26b-3p (Duplex Sequences: 5'-/5Phos/rCrCrUrGrUrUrCrUrCrCrArUrUrArCrUrUrGrGmCmUrC-3' and 5'-mGmCrCmArAmGrUmArAmUrGmGrAmGrAmArCmArGG-3') and miR-26b-5p (Duplex Sequences: 5'-/5Phos/rUrUrCrArArGrUrArArUrUrCrArGrGrArUrAmGmGrU-

3' and 5'-mCmUrAmUrCmCrUmGrAmArUmUrAmCrUmUrGmAA-3') mimics (IDT). The medium was refreshed every 24 hours. The slices were collected to check the viability of the slices by measuring ATP levels and supernatant was collected for further analysis.

2.14 MiR-26b expression in patient cohort

All patients were prospectively recruited in the Department of Medicine II (Saarland University Medical Center, Homburg, Germany) between December 2021 and March 2023. Included patients were adults and had either type 1 or type 2 diabetes. Alcohol consumption above the National Institute on Alcohol Abuse and Alcoholism's (NIAAA) definition of chronic alcohol use (four drinks or more on any day or 14 drinks per week for men or three drinks or more on any day or 7 drinks per week for women) was regarded as exclusion criterium. Serum and EDTA blood samples were collected from fasted patients. Genomic DNA was isolated from EDTA anticoagulated blood according to the membrane-based QIAamp DNA extraction protocol (Qiagen, Hilden, Germany). The common genetic variants involved known to modulate the risk of fatty liver, namely *PNPLA3*, *TM6SF2*, *MBOAT7*, *SERPINA*, *HSD17B13*, and *MTARC1*, were genotyped using a solution-phase hybridization reaction with 5'-nuclease and fluorescence detection. Transient elastography (TE) and controlled attenuation parameter (CAP) were performed to non-invasively quantify liver fibrosis and steatosis, respectively. Cirrhosis was defined by TE greater or equal 15 kPa, and fibrosis F0 was defined by TE below 6,5 kPa [13, 14].

RNA was isolated from 100µl serum, using the miRNeasy serum/plasma kit (Qiagen), according to the manufacturer's instructions. C. elegans miR-39 miRNA mimic was added as spike-in control. Subsequently, cDNA was generated using the TaqMan

MicroRNA Reverse Transcription Kit (ThermoFisher) according to the manufacturer's instructions using 10ng of total RNA. The relative gene expression levels were determined by quantitative polymerase chain reaction (qPCR) using TaqMan MicroRNA-assays (ThermoFisher) for miR-39 (Assay-ID: 000200), miR-26b-3p (Assay-ID: 000407) or miR-26b-5p (Assay-ID: 002444). For the qPCR reaction, 0.5ng of cDNA template was used to which TaqMan gene expression master mix (ThermoFisher) and above-described primers were added. PCR cycling was performed on QuantStudio 3 Real-Time PCR system (ThermoFisher) with the following conditions: 50˚C for 2min for 1 cycle (UDG activation); 95˚C for 10min for 1 cycle (Dual-Lock DNA polymerase); and 95˚C for 15sec (Denature), 60˚C for 60sec (Anneal/Extend) for 40 cycles. Expression of miR-39 as spike-in control was used for normalization.

2.15 Statistics

Statistical analysis was performed using GraphPad Prism version 9.1.1 (GraphPad Software, Inc., San Diego, CA, USA). Outliers were identified using the ROUT = 1 method after which normality was tested via the D'Agostino-Pearson and Shapiro-Wilk normality test. Significance was tested using either Welch's t-test for normally distributed data or Mann-Whitney U test for non-normally distributed data. All data are expressed as mean ± standard error of the mean (SEM) and results of <0.05 for the *p*-value were considered statistically significant.

All authors had access to the study data and have reviewed and approved the final manuscript.

3. RESULTS

3.1 Mice deficient in *miR-26b* show increased hepatic lipid levels and an increased expression of hepatic lipid uptake receptors.

To determine the role of miR-26b in hepatic lipid metabolism and MASH development, hepatic cholesterol and triglyceride levels were measured in *Apoe*$^{-/-}$ and *Apoe*$^{-/-}$*Mir26b*$^{-/-}$ mice that were fed a 4-week WTD (**Figure 1A**). Total cholesterol and triglyceride levels were significantly increased in the livers of *Apoe*$^{-/-}$*Mir26b*$^{-/-}$ mice compared to control mice (**Figure 1B-C**). This hepatic lipid effect was also confirmed by Oil-red-O staining, showing increased lipid accumulation in the livers of *Apoe*$^{-/-}$*Mir26b*$^{-/-}$ mice (**Figure 1D-E**). Moreover, pathological scoring of the Oil-red-O staining unveiled that the *Apoe*$^{-/-}$*Mir26b*$^{-/-}$ mice showed a clear tendency towards increased steatosis compared to controls, especially of macrovesicular steatosis (**Figure 1F**).

To elucidate possible mechanisms underlying the increased hepatic lipid levels, gene expression levels of key proteins involved in lipid metabolism were measured in liver tissues of *Apoe*$^{-/-}$ and *Apoe*$^{-/-}$*Mir26b*$^{-/-}$ mice. Notably, a knockout of miR-26b did not affect the expression levels of 'ATP binding cassette subfamily A member 1' (*Abca1*) or 'acetyl-CoA acetyltransferase 2' (*Acat2*) (**Figure 1G-H**). However, livers of *Apoe*$^{-/-}$ *Mir26b*$^{-/-}$ mice showed a clearly increased expression of scavenger receptor *Cd36* (**Figure 1I**) and a striking 2-fold increase of the expression of scavenger receptor A (*Sra*) (**Figure 1J**). This could also be validated on protein level, by showing increased CD36 as well as SRA expression in livers of *Apoe*$^{-/-}$*Mir26b*$^{-/-}$ mice (**Figure 1K-L**). Since these scavenger receptors are highly expressed on macrophages, we have

evaluated the contribution of myeloid miR-26b to the observed hepatic lipid effects. Interestingly, mice that have a myeloid-specific lack of *miR-26b* also show increased hepatic cholesterol levels and lipid accumulation demonstrated by Oil-red-O staining, coinciding with an increased hepatic *Cd36* expression (**Figure 2**), demonstrating that myeloid miR-26b plays a major, but not exclusive, role in the observed steatosis.

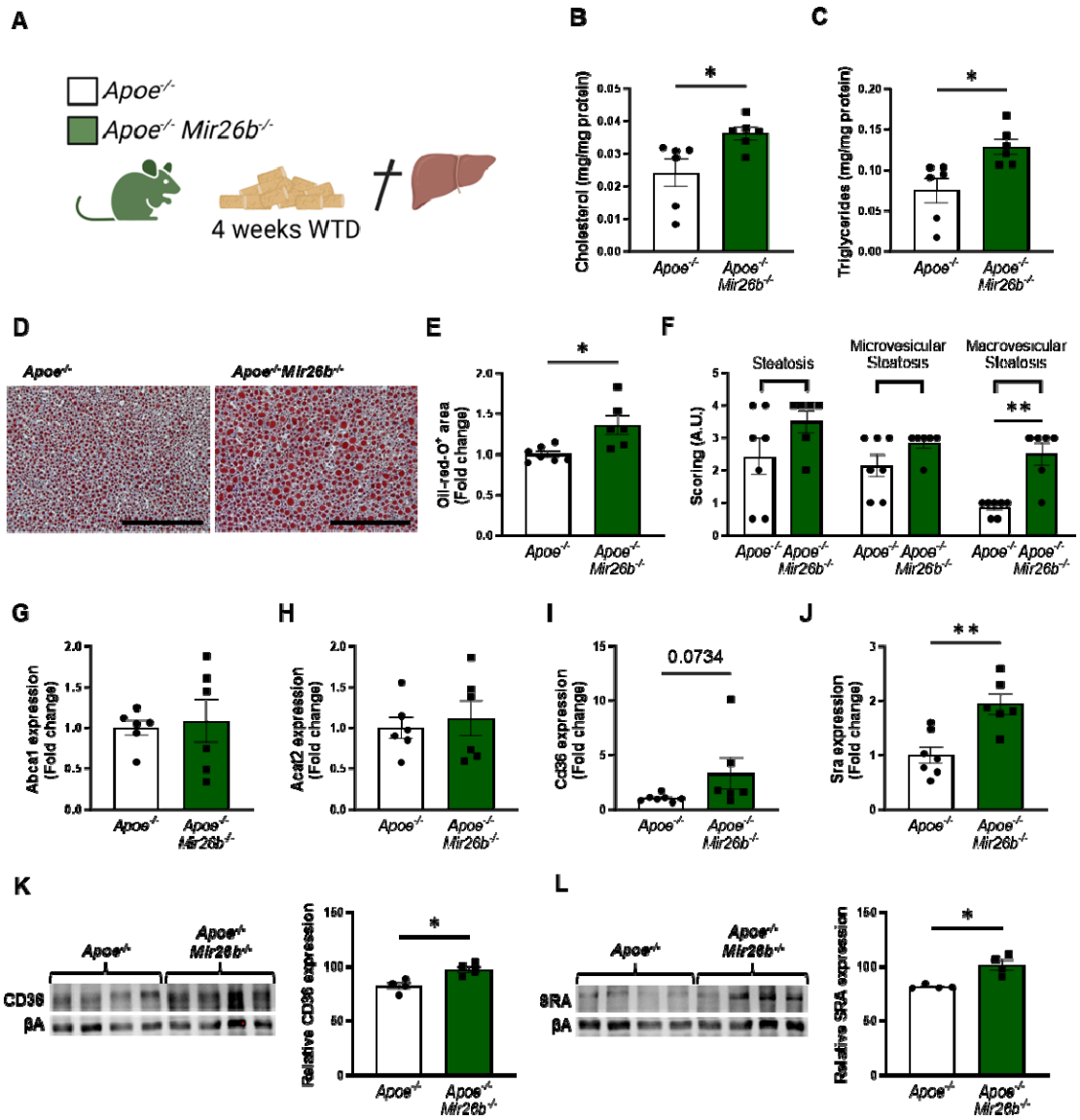

Figure 1. Hepatic lipid levels and the expression of lipid uptake receptors are increased by a whole-body knockout of miR-26b in mice.

(**A**) Schematic overview of the experimental approach. (**B-C**) Hepatic total cholesterol (**B**) and triglyceride (**C**) measurements normalized against total protein. (**D**) Representative pictures of Oil-red-O staining of liver sections. Scale bar=200µm. (**E**) Quantification of the Oil-red-O staining. (**F**) Pathological scoring of the Oil-red-O staining. (**G-J**) Gene expression analysis of (**G**) *Abca1*, (**H**) *Acat2*, (**I**) *Cd36*, and (**J**) *Sra*. (**K-L**) Western-blot analysis and quantification of (**K**) CD36 and (**L**) SRA. Fold change is corrected for sex. *p<0.05; **p<0.01. n=4-7 animals per group.

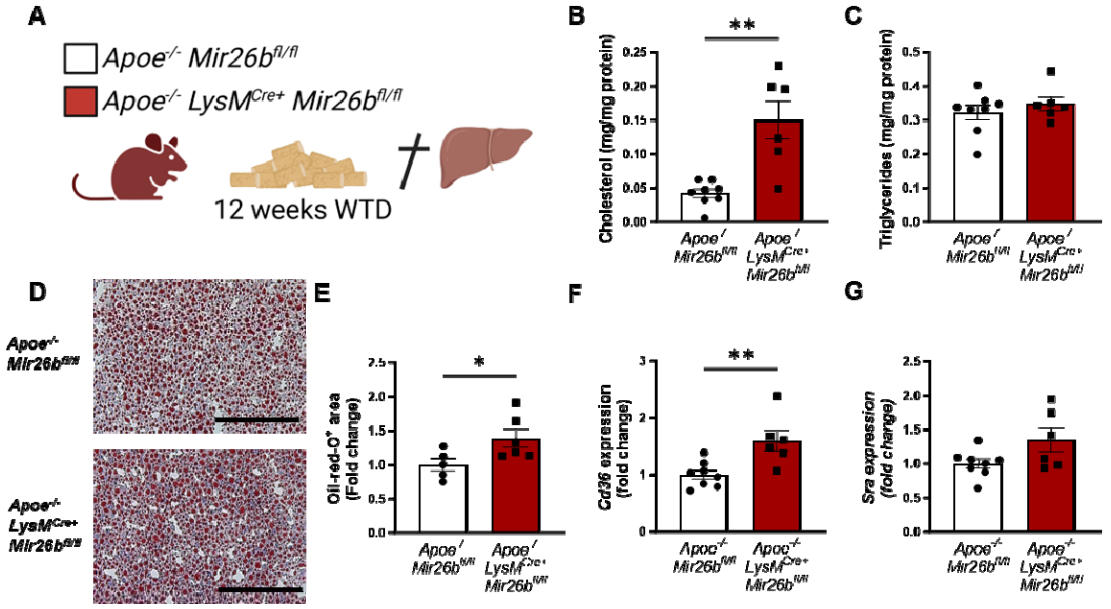

Figure 2. Hepatic lipid levels and the expression of lipid uptake receptors are increased by a myeloid-specific *miR-26b* deficiency in mice.

(**A**) Schematic overview of the experimental approach. (**B-C**) Hepatic total cholesterol (**B**) and triglyceride (**C**) measurements normalized against total protein. (**D**) Representative pictures of Oil-red-O staining of liver sections. Scale bar=200µm. (**E**) Quantification of the Oil-red-O staining. (**F-G**) Gene expression analysis of (**F**) *Cd36* and (**G**) *Sra*. Fold change is corrected for sex. **p*<0.05; ***p*<0.01. *n*=6-8 animals per group.

3.2 Livers of *miR-26b* knockout mice have higher levels of inflammatory cytokines and an increased number of infiltrating macrophages.

Besides lipid accumulation, an increased inflammatory profile is a key characteristic of MASH [2]. Therefore, we aimed to elucidate the role of miR-26b in hepatic inflammation. Hepatic protein levels of the pro-inflammatory cytokines IL-6 and TNF were significantly increased in *Apoe*$^{-/-}$*Mir26b*$^{-/-}$ mice compared to controls (**Figure 3A-B**), while levels of the chemokines CCL2 and CXCL1 remained unchanged (**Figure 3C-D**). To further investigate the effects of the whole-body knockout on a cellular level, liver sections were stained to identify several key leukocyte subpopulations.

Mac-1-positive cells were significantly increased in livers of mice lacking *miR-26b*, indicating a higher infiltration of macrophages and neutrophils (**Figure 3E**). To identify whether the increase of Mac-1-positive cells is due to macrophage or neutrophil infiltration we also determined the number of Ly6G-positive cells, which remained unchanged, suggesting that the increased number of Mac-1 positive cells was likely the result of an increase in the number of infiltrating macrophages rather than neutrophils (**Figure 3F**). Furthermore, the whole-body knockout of *miR-26b* only affected the number of infiltrating macrophages and not Kupffer cells, which are recognized as CD68-positive cells (**Figure 3G)**. Furthermore, the number of CD3-positive cells did not differ between *Apoe*$^{-/-}$*Mir26b*$^{-/-}$ mice and controls (**Figure 3H**), suggesting that miR-26b does not affect T-cell counts in the liver.

Collectively, these results indicate that miR-26b plays a protective role in hepatic inflammation by influencing TNF and IL-6 levels and macrophage infiltration in the liver.

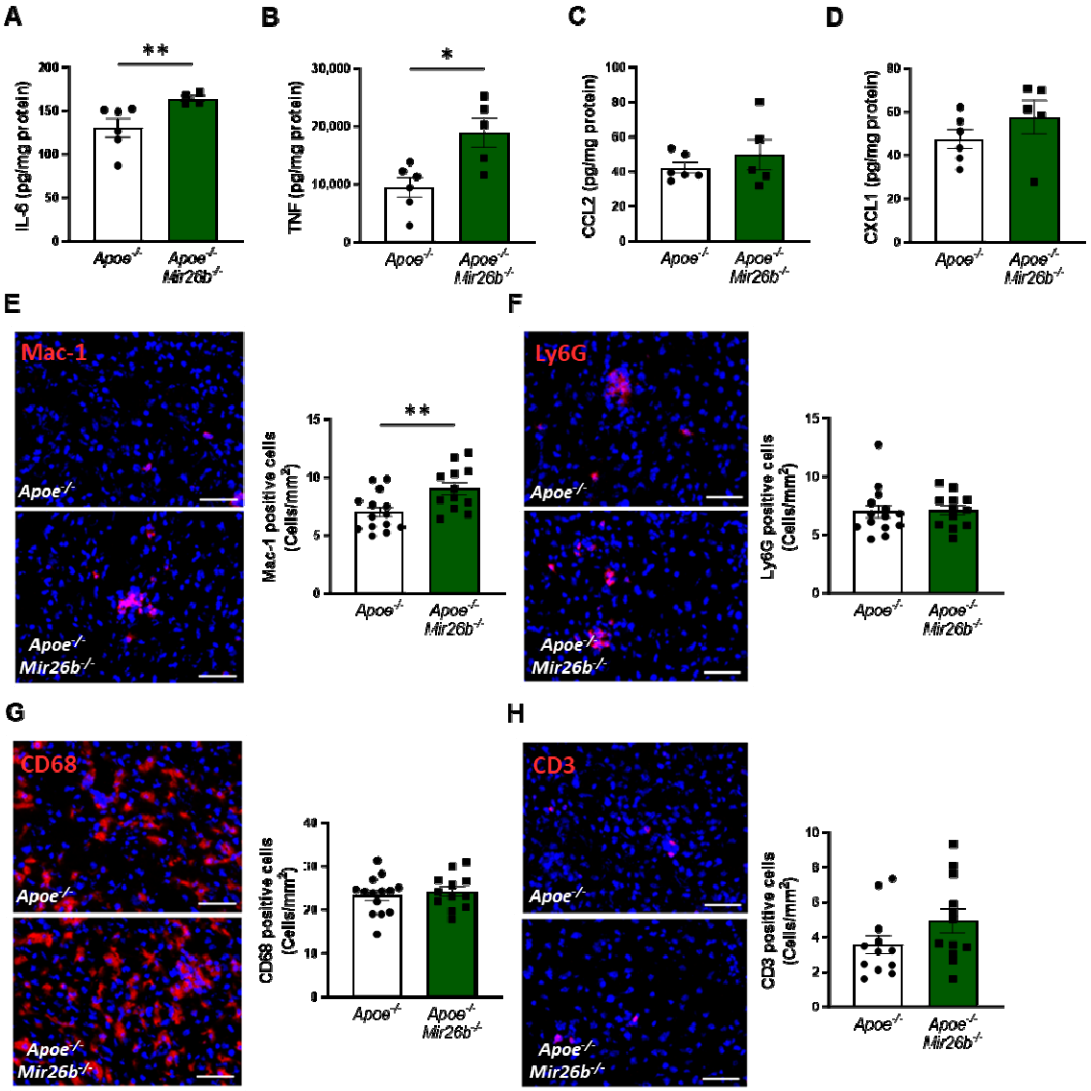

Figure 3. Livers of *Apoe*$^{-/-}$*Mir26b*$^{-/-}$ mice show elevated pro-inflammatory cytokine levels and an increased number of Mac-1-positive cells.

(**A-D**) Cytokine levels of (**A**) IL-6, (**B**) TNF, (**C**) CCL2, and (**D**) CXCL1 were measured in liver protein lysates. (**E-H**) Representative images and quantification of immunofluorescent stainings for (**E**) infiltrating macrophages and neutrophils (Mac-1), (**F**) neutrophils (Ly6G), (**G**) resident monocytes/macrophages (CD68), and (**H**) T-cells (CD3). Scale bar=50µm. *p<0.05; **p<0.01. n=6-7 animals per group.

3.3 A knockout of *miR-26b* in mice results in increased hepatic fibrosis, which coincides with an increased expression of *Tgfb*.

Continued hepatic inflammation can cause fibrotic changes in the liver, which is another characteristic of MASH [2]. As such, we also investigated the influence of miR-26b on hepatic fibrosis in mice. Collagen deposition in liver sections was determined by a Sirius-red staining, which showed that a knockout of *miR-26b* significantly exacerbated hepatic fibrosis (**Figure 4A-B**). This was further supported by the increased expression of 'transforming growth factor β' (*Tgfb*) in the livers of *Apoe*$^{-/-}$*Mir26b*$^{-/-}$ mice compared to controls (**Figure 4C**). Another gene involved in liver fibrosis, i.e. 'actin alpha 2' (*Acta2)*, trended towards an elevated expression in mice lacking miR-26b (**Figure 4D**). Lastly, a whole-body knockout of miR-26b resulted in an increased expression of 'matrix metalloproteinase 13' (*Mmp13)* (**Figure 4E**). Overall, these results imply a protective role of miR-26b in liver fibrosis, which is linked to an altered expression of *Tgfb*.

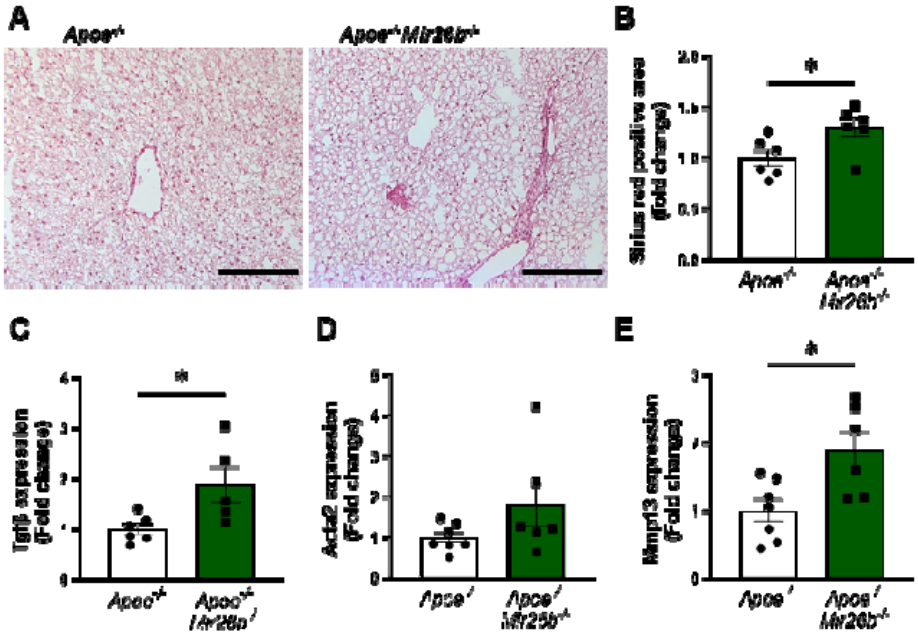

Figure 4. Livers of *Apoe*$^{-/-}$*Mir26b*$^{-/-}$ mice show increased hepatic fibrosis.

(**A**) Representative pictures of Sirius-red staining of liver sections. Scale bar=100µm. (**B**) Quantification of the Sirius-red staining. (**C-E**) Gene expression of (**C**) *Tgfb*, (**D**) *Acta2*, and (**E**) *Mmp13*. Fold change is corrected for sex. *p<0.05. n=6-7 animals per group.

3.4 Liver of *miR-26b* knockout mice show highly increased kinase activity related to inflammatory pathways.

To elucidate the underlying mechanisms behind the effects of miR-26b on the liver, we have performed a kinase activity profiling, focusing on serine-threonine kinases (STK). In order to evaluate the differentially activated kinases, the degree of phosphorylation of peptides coated on STK arrays is determined. Liver lysates from *Apoe*$^{-/-}$*Mir26b*$^{-/-}$ mice (KO) showed a strong and very distinct upregulation of peptide phosphorylation compared to liver lysates from *Apoe*$^{-/-}$ mice (WT) (**Figure 5A-B** and **Supplemental Figure 1A**). Remarkably, 84 kinases were significantly more activated in liver lysates from *Apoe*$^{-/-}$*Mir26b*$^{-/-}$ mice compared to controls (**Figure 5C**), many of which are involved in inflammatory pathways such as c-Jun-N-terminal kinases (JNKs), mitogen-activated protein kinases (MAPKs), and extracellular-signal, regulated kinases (ERKs). This was also further corroborated by pathway analysis (**Figure 5D-E**), showing enrichment in pathways related to inflammation (e.g. MAP kinase activation, TLR signaling) and angiogenesis (e.g. VEGF signaling). Combined, these results demonstrate that the lack of *miR-26b* increases kinase activity in the liver, particularly of kinases related to inflammatory pathways, which can thus be a plausible mechanism behind the hepatic effects observed in *miR-26b* deficient mice.

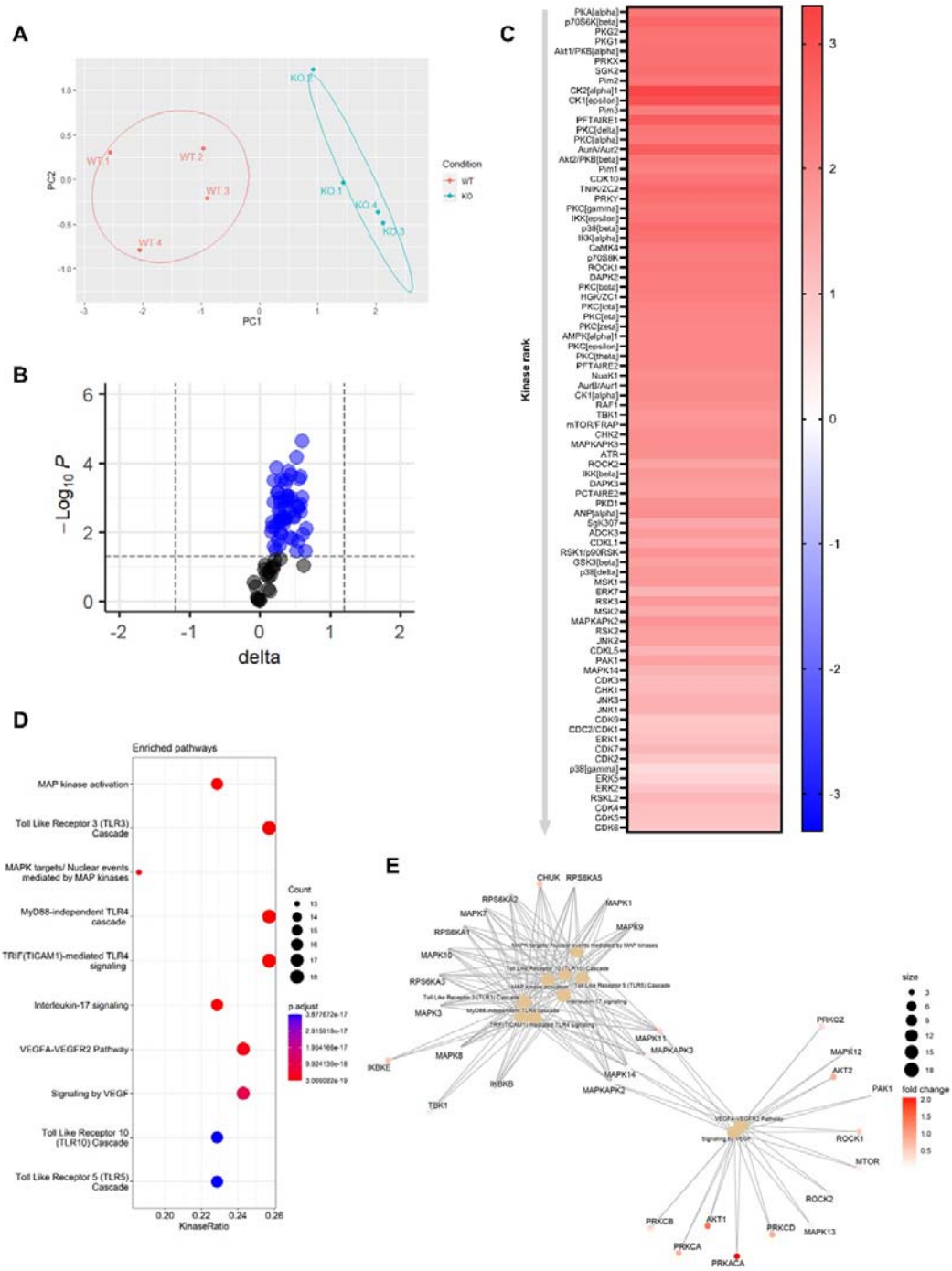

Figure 5. Knockout of *miR-26b* results in an increased hepatic inflammatory kinase activity.

(**A**) Principal component analysis (PCA) of phosphorylated peptides from STK array (n=4) of liver lysates from *Apoe*$^{-/-}$*Mir26b*$^{-/-}$ mice (KO) or *Apoe*$^{-/-}$ (WT) mice**.** (**B**) Volcano plot visualizing fold change and *p*-value for phosphorylated peptides from STK array. Blue dots represent significantly altered phosphopeptides. (**C**) Heatmap of significantly changed kinases are ranked based on Median Final Score (cut-off value of 1.2), STK array performed on liver lysates from *Apoe*$^{-/-}$*Mir26b*$^{-/-}$ mice (KO)

compared to *Apoe*$^{-/-}$ (WT) mice**.** Color corresponds to the Median Kinase Statistic, which represents effect size and directionality (red = increased activity in KO vs. WT mice). (**D**) Enriched Pathways based on STK array. (**E**) Network diagram of the pathway enrichment analysis.

3.5 Lipid nanoparticles loaded with miR-26b mimics can partly rescue the MASH phenotype in whole-body *miR-26b* knockout mice.

Since the whole-body knockout mouse model demonstrated that miR-26b plays a role in MASH, we attempted to rescue the phenotype by injecting *Apoe*$^{-/-}$*Mir26b*$^{-/-}$ mice on WTD with LNPs, which act as clinically and therapeutically relevant vehicles [8], loaded with miR-26b mimics (mLNPs) and empty lipid nanoparticles (eLNPs) as control for 4 weeks (**Figure 6A**). These mLNPs overexpress the miR-26b level in the whole-body deficient mouse (**Supplemental Figure 2A-B**), providing insight into the therapeutic potential of miR-26b. Injections with mLNPs lowered hepatic cholesterol levels compared to the vehicle control (**Figure 6B**), whilst triglyceride levels remained unaffected (**Figure 6C**). These findings were further confirmed by demonstrating that treatment with mLNPs significantly reduced the Oil-red-O positive area (**Figure 6D-E**). While mLNP treatment did not affect *Cd36* expression (**Figure 6F**), it resulted in a 0.67-fold reduction in *Sra* expression compared to mice injected with eLNPs (**Figure 6G**). Although mLNP treatment affects hepatic lipid levels, no changes could be observed on hepatic inflammation, characterized by inflammatory cytokines and infiltrated myeloid cells, or fibrosis (**Figure 6H-L**). However, expression of *Tgfb* was significantly reduced upon mLNP treatment (**Figure 6M**), coinciding with a tendency to decreased *Mmp13* expression (**Figure 6N**). These changes on gene expression suggest that the mLNP treatment might have been to short to observe pronounced effects on later stages of disease development like inflammation and fibrosis.

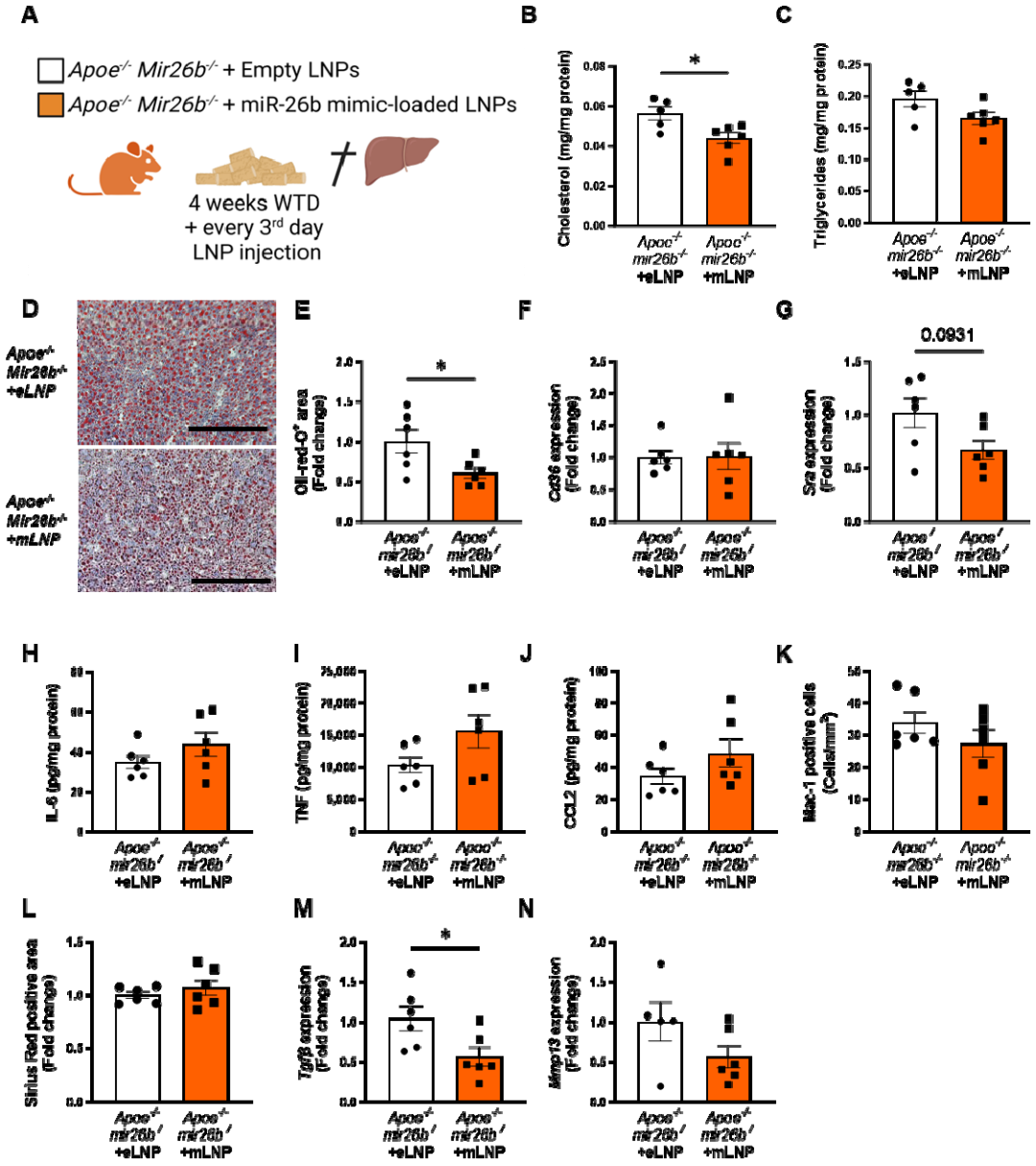

Figure 6. *Apoe*$^{-/-}$*Mir26b*$^{-/-}$ mice injected with LNPs containing miR-26b mimics show decreased hepatic lipid levels compared to vehicle control injected mice.

(**A**) Schematic overview of the experimental approach in which mice on 4-week WTD were simultaneously injected every 3 days with either empty LNPs as vehicle control (eLNP) or LNPs containing miR-26b mimics (mLNP). (**B-C**) Hepatic total cholesterol (**B**) and triglyceride (**C**) measurements normalized against total protein. (**D**) Representative pictures of Oil-red-O staining of liver sections. Scale bar=200µm. (**E**) Quantification of the Oil-red-O staining. (**F-G**) Gene expression analysis of (**F**) *Cd36* and (**G**) *Sra*. (**H-J**) Cytokine levels of (**H**) IL-6, (**I**) TNF, and (**J**) CCL2 were measured in liver protein lysates. (**K**) Quantification of immunofluorescent staining for infiltrating

macrophages and neutrophils (Mac-1). (**L**) Quantification of the Sirius-red staining. (**M-N**) Gene expression of (**M**) *Tgfb*, and (**N**) *Mmp13*. Fold change is corrected for sex. *$p<0.05$. $n=6$ animals per group.

Furthermore, kinase activity profiling of liver lysates demonstrated a distinct downregulation of peptide phosphorylation upon mLNP treatment of *Apoe*$^{-/-}$*Mir26b*$^{-/-}$ (KO.LNP) mice (**Figure 7A-B** and **Supplemental Figure 1A-B**). Interestingly, principal component analysis (PCA) clearly demonstrated that livers from mLNP-treated *Apoe*$^{-/-}$*Mir26b*$^{-/-}$ (KO.LNP) mice more closely resembled *Apoe*$^{-/-}$ (WT) mice rather than *Apoe*$^{-/-}$*Mir26b*$^{-/-}$ (KO) mice (**Figure 7A**). The kinase activity of 76 kinases in the liver was significantly downregulated upon mLNP treatment of *Apoe*$^{-/-}$*Mir26b*$^{-/-}$ mice (**Supplemental Figure 1C**). The notion that 60 (79%) of these downregulated kinases were originally upregulated by the *miR-26b* deficiency (**Figure 7C**), furthermore indicates that mLNP treatment rescues the observed effects due to the *miR-26b* deficiency. In line with this, pathway analysis also showed an enrichment of similar pathways as described before, i.e. pathways related to inflammation and angiogenesis (**Figure 7D-E**), again demonstrating that there are at least already early signs that inflammation is influenced by mLNP treatment.

Overall, treatment with mLNPs attenuated MASH development with regard to hepatic lipids and inflammatory kinase activity, highlighting the therapeutic potential of LNPs loaded with miR-26b mimics.

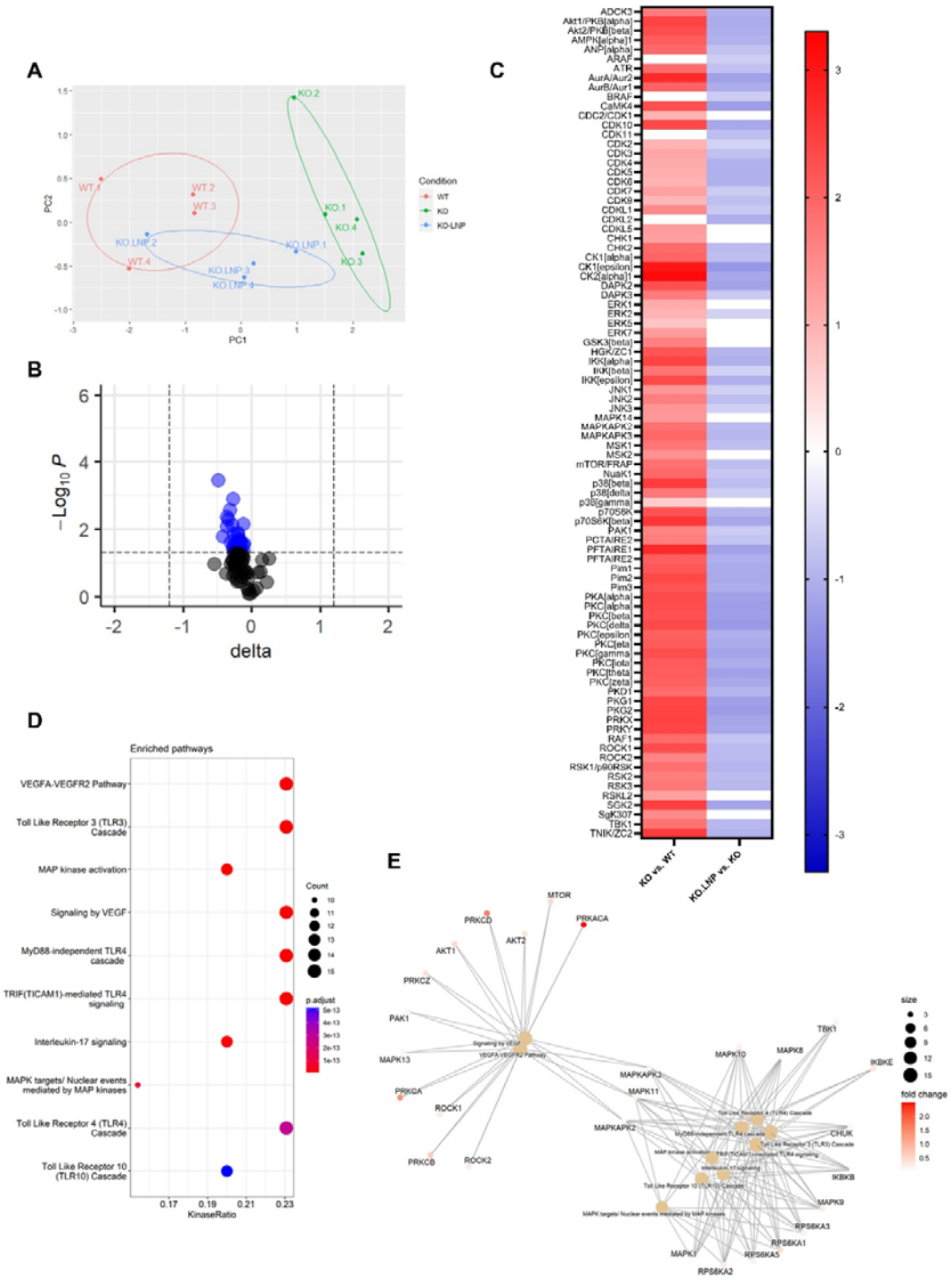

Figure 7. mLNP treatment of *miR-26b* knockout mice results in a decreased hepatic inflammatory kinase activity.

(**A**) Principal component analysis (PCA) of phosphorylated peptides from STK array (n=4) of liver lysates from mLNP treated *Apoe*$^{-/-}$*Mir26b*$^{-/-}$ mice (KO.LNP), *Apoe*$^{-/-}$*Mir26b*$^{-/-}$ mice (KO) or *Apoe*$^{-/-}$ mice (WT) mice**.** (**B**) Volcano plot visualizing fold change and P value for phosphorylated peptides from

STK array. Blue dots represent significantly altered phosphopeptides. (**C**) The heatmap of significantly changed kinases is ranked based on the Median Final Score (cut-off value of 1.2). Color is corresponding to Median Kinase Statistic, which represents effect size and directionality (red = increased activity in KO vs. WT mice; blue = decreased activity in KO.LNP vs. KO mice) (average of n=4 is shown). (**D**) Enriched Pathways based on STK array. (**E**) Network diagram of the pathway enrichment analysis.

3.6 Lipid nanoparticles loaded with miR-26b mimics have anti-inflammatory effects on human livers.

Since the mouse experiments demonstrated a clear therapeutic potential of LNPs loaded with miR-26b mimics, we also set out to explore this potential in a human setting. Human precision-cut liver slices were cultured for 24h or 48h in the presence of mLNPs or eLNPs as control (**Figure 8A**). Although no effects were observed on IL-6 secretion (**Figure 8B**), mLNPs had strong anti-inflammatory effects on these human precision-cut liver slices. The secretion of TNF, CCL2, and CXCL1 was significantly reduced in slices treated with mLNPs compared to eLNP-treated liver slices (**Figure 8C-E**), underlining the clear potential of these miR-26b-loaded LNPs in a human context.

To further evaluate the importance of miR-26b in liver diseases in humans, we have measured the expression levels of miR-26b-3p and miR-26b-5p in the plasma of healthy subjects and patients with liver cirrhosis (**Figure 8F**). Remarkably, both miR-26b-3p and -5p were significantly elevated in the plasma of liver cirrhosis patients (**Figure 8G-H**), suggesting -at least- a strong association between miR-26b and the development of MASH in humans.

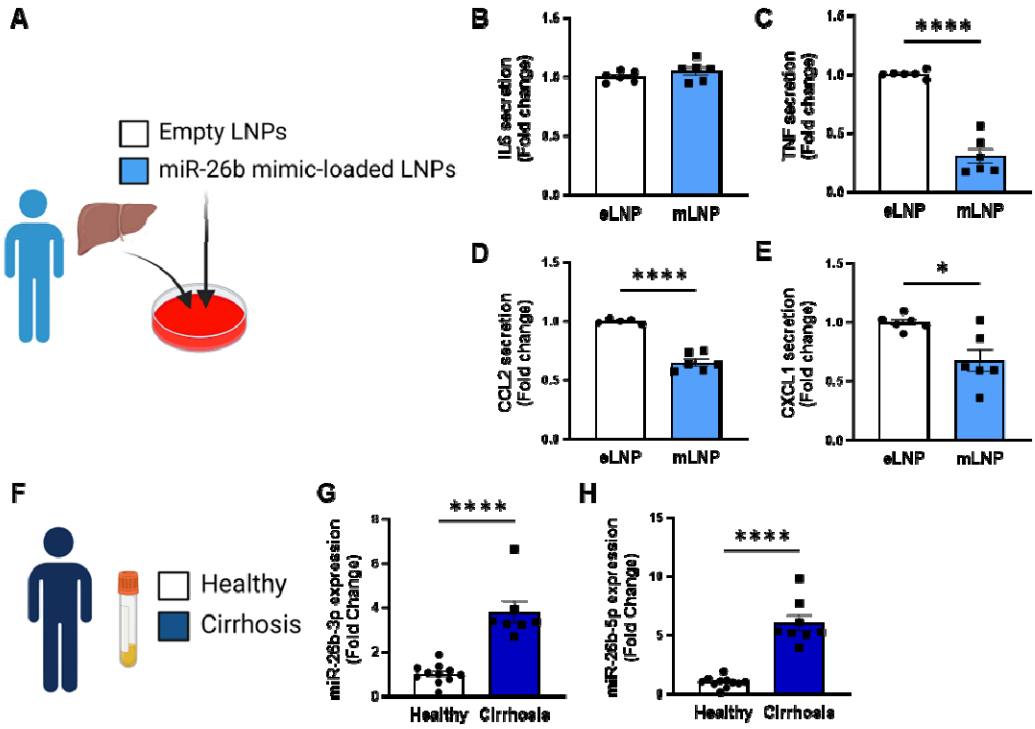

Figure 8. MiR-26b-loaded LNPs have anti-inflammatory effects on human liver slices and miR-26b plasma levels are significantly increased in patients with liver cirrhosis.

(**A**) Schematic overview of the experimental approach. (**B-E**) Cytokine levels of (**B**) IL-6, (**C**) TNF, (**D**) CCL2, and (**E**) CXCL1 measured in the supernatant of human precision-cut liver slices after 24h (for IL-6/TNF) or 48h (for CCL2/CXCL1) incubation with mLNPs or eLNPs (3 individual donors, cultured in duplicates). (**F-G**) Plasma was isolated from patients with liver cirrhosis or healthy volunteers (**F**) and miR-26b-3p (**G**) and miR-26b-5p (**H**) plasma levels were measured. *p<0.05; ****p<0.0001. n=8-11 patients per group.

4. DISCUSSION

MiRs have been indicated to play a critical role in the development of several pathologies, including MASH. While the role of miR-26b has already been investigated in various cardio-metabolic diseases [5], its role in MASH remained unknown so far. Therefore, this study focused on the role of miR-26b in MASH showing that mice deficient in miR-26b presented with a higher hepatic lipid content, higher levels of pro-inflammatory cytokines, and an increased number of infiltrated macrophages in the liver and exacerbated hepatic fibrosis. This coincided with an increased activity of kinases that are involved in inflammatory pathways. Finally, when attempting to rescue this phenotype by injecting LNPs loaded with miR-26b mimics, we managed to decrease hepatic cholesterol, overall hepatic lipid levels, gene expression of *Sra*, and the activity of inflammatory kinases. These anti-inflammatory effects of miR-26b loaded LNPs were also confirmed in human precision-cut liver slices. Taken together, these results suggest that miR-26b plays a protective role in MASH development and shows the therapeutic potential of miR-26b loaded LNPs.

In this study, *Apoe*$^{-/-}$*Mir26b*$^{-/-}$ mice showed elevated hepatic cholesterol and triglyceride levels, which coincided with increased expression of *Sra* and *Cd36*. Generally, SR-A and CD36 play a critical role in lipid metabolism, as 75% to 90% of oxidized low-density lipoprotein (ox-LDL) is taken up by macrophages via these receptors [15]. In line with our observations, previous studies already highlighted that CD36 and SR-A play a key role in MASH development. For example, a hematopoietic deficiency of these receptors resulted in reduced hepatic inflammation [16]. Furthermore, a recent study demonstrated that mice lacking SR-A show

decreased hepatic lipid levels and inflammation [17]. Interestingly, they also demonstrated that SR-A induced JNK signaling [17], which is also in line with our kinase activity results. Moreover, it could be demonstrated that *CD36* expression is upregulated in the livers of MASLD patients, leading to hepatic triglyceride accumulation and consequently an exacerbation of hepatic steatosis [18]. Overall, this strongly indicates that an increased hepatic expression of *Cd36* and *Sra* in both mice and humans causes hepatic cholesterol and triglyceride accumulation as well as inflammation, adding fuel to the notion of CD36 and SR-A as a possible underlying mechanism through which miR-26b exerts its effects on MASH development.

Elevated hepatic lipid levels lead to the release of pro-inflammatory cytokines, consequently mediating liver injury and inflammation in MASH [19], which could also be observed in our study. The elevated levels of pro-inflammatory cytokines in the liver led to the increased number of Mac-1 positive cells, representing infiltrated macrophages. The production of IL-6 and TNF by macrophages in turn led to further local inflammation, also highlighted by the increased inflammatory kinase activity in the liver, thereby causing a vicious cycle of cytokine release and myeloid cell infiltration[20]. Interestingly, TNF has been shown to promote steatosis by altering lipid metabolism and inducing fatty acid uptake in the liver [21, 22], further showing the critical link between inflammation and hyperlipidemia. Additionally, infiltrated macrophages usually form clusters, especially in areas of macrovesicular steatosis [23], which was in line with our current study. Overall, these findings indicate a crosstalk between hepatic lipid levels, inflammation, and macrophage infiltration and show that miR-26b might play a protective role in these processes.

The third characteristic of MASH that was investigated during this study was hepatic fibrogenesis. Hepatic fibrosis is mainly caused by the activation of the fibrogenic factor TGF-β [24], which is also confirmed in the current study as miR-26b knockout mice displayed a higher amount of Sirius red positive area and an increased expression of *Tgfb*. Additionally, *Mmp13*, a protein responsible for extracellular matrix degradation, was upregulated in *Apoe*$^{-/-}$*Mir26b*$^{-/-}$ mice, which is probably a secondary compensatory response to the increase in fibrosis. Besides this, MMP13 has been shown to play a less straightforward role in liver fibrosis [25]. Uchinami *et al.* demonstrated that levels of TNF and TGF-β were suppressed in MMP13-deficient mice in an early phase of liver fibrosis, suggesting that MMP13 possibly accelerates hepatic fibrogenesis by mediating inflammation. Overall, this indicates that miR-26b plays a protective role in hepatic fibrogenesis, possibly due to modulating TGF-β and MMP13 levels.

Finally, to study the therapeutic potential of miR-26b, we injected whole-body knockout mice with miR-26b mimic-loaded LNPs. LNP-based therapies have emerged over the last few years and have been extensively studied and even already used in clinical settings [26], underlining the translatability and potential of our study. Interestingly, the LNP treatment not only showed significant results on hepatic lipid metabolism but also reversed the effects on inflammatory kinase activity, particularly of pathways mediated by key regulators like JNKs, MAPKs and ERKs. However, the LNP treatment did not seem to affect the inflammatory cytokine, cellular leukocyte influx or fibrosis in the liver, suggesting that the treatment might be to short to see such functional effects on later disease stages. Nonetheless, a note of caution is the fact that we injected the LNPs simultaneously with the diet, providing a more preventative approach as opposed to a curative therapy. Furthermore, we

demonstrated that miR-26b loaded LNPs have anti-inflammatory effects on human precision-cut liver slices, which, combined with the suppressed levels of cholesterol and hepatic lipids in our mouse model, underline its potential as an exciting therapeutic option.

Besides the *in vivo* studies, we also examined the expression levels of miR-26b in the plasma of liver cirrhosis patients. Compared to healthy subjects, both miR-26b-3p and -5p were expressed higher in patients with liver cirrhosis. This is in contrast to our mouse model in which higher expression levels led to a more beneficial phenotype. Important to note is that the levels of miR-26b in the plasma of these patients do not prove causality. The increase in miR-26b expression could be due to a mechanism in which the body attempts to rescue the diseased phenotype. This would make the miR an interesting target as a biomarker though. However, more research should be conducted as the size of the human study is rather limited and only focuses on one of the last stages of MASLD.

Collectively, these results show that miR-26b plays a protective role in the development of MASH by exerting effects on hepatic lipid metabolism, inflammation, and fibrosis. Future research should focus on the further clinical translation of our results by evaluating the effects of miR-26b loaded LNPs on various human tissues. Overall, we show here thought-provoking results on the role of miR-26b in MASH development and highlight this miR as a promising therapeutic target, providing a solid base for exciting future research.

Acknowledgements

Schematic overview figures are made with Biorender.

References

1. Eslam M, Sanyal AJ, George J, International Consensus P. MAFLD: A Consensus-Driven Proposed Nomenclature for Metabolic Associated Fatty Liver Disease. Gastroenterology. 2020;158(7):1999-2014 e1.

2. Peng C, Stewart AG, Woodman OL, Ritchie RH, Qin CX. Non-Alcoholic Steatohepatitis: A Review of Its Mechanism, Models and Medical Treatments. Front Pharmacol. 2020;11:603926.

3. Gjorgjieva M, Sobolewski C, Dolicka D, Correia de Sousa M, Foti M. miRNAs and NAFLD: from pathophysiology to therapy. Gut. 2019;68(11):2065-79.

4. Lopez-Sanchez GN, Dominguez-Perez M, Uribe M, Chavez-Tapia NC, Nuno-Lambarri N. Non-alcoholic fatty liver disease and microRNAs expression, how it affects the development and progression of the disease. Ann Hepatol. 2021;21:100212.

5. van der Vorst EPC, Pepe MAA, Peters LJF, Haberbosch M, Jansen Y, Naumann R, Stathopoulos GT, Weber C, Bidzhekov K. Transcriptome signature of miRNA-26b KO mouse model suggests novel targets. BMC Genom Data. 2021;22(1):23.

6. Zhao N, Wang R, Zhou L, Zhu Y, Gong J, Zhuang S-M. MicroRNA-26b suppresses the NF-κB signaling and enhances the chemosensitivity of hepatocellular carcinoma cells by targeting TAK1 and TAB3. Molecular Cancer. 2014;13(1):35.

7. Yang L, Dong C, Yang J, Yang L, Chang N, Qi C, Li L. MicroRNA-26b-5p Inhibits Mouse Liver Fibrogenesis and Angiogenesis by Targeting PDGF Receptor-Beta. Molecular Therapy - Nucleic Acids. 2019;16:206-17.

8. Jeong M, Lee Y, Park J, Jung H, Lee H. Lipid nanoparticles (LNPs) for in vivo RNA delivery and their breakthrough technology for future applications. Adv Drug Deliv Rev. 2023;200:114990.

9. Yu G, Wang LG, Yan GR, He QY. DOSE: an R/Bioconductor package for disease ontology semantic and enrichment analysis. Bioinformatics. 2015;31(4):608-9.

10. Yu G, He QY. ReactomePA: an R/Bioconductor package for reactome pathway analysis and visualization. Mol Biosyst. 2016;12(2):477-9.

11. de Graaf IA, Olinga P, de Jager MH, Merema MT, de Kanter R, van de Kerkhof EG, Groothuis GM. Preparation and incubation of precision-cut liver and intestinal slices for application in drug metabolism and toxicity studies. Nat Protoc. 2010;5(9):1540-51.

12. Simon E, Motyka M, Prins GH, Li M, Rust W, Kauschke S, Viollet C, Olinga P, Oldenburger A. Transcriptomic profiling of induced steatosis in human and mouse precision-cut liver slices. Sci Data. 2023;10(1):304.

13. Mozes FE, Lee JA, Selvaraj EA, Jayaswal ANA, Trauner M, Boursier J, Fournier C, Staufer K, Stauber RE, Bugianesi E, Younes R, Gaia S, Lupsor-Platon M, Petta S, Shima T, Okanoue T, Mahadeva S, Chan WK, Eddowes PJ, Hirschfield GM, Newsome PN, Wong VW, de Ledinghen V, Fan J, Shen F, Cobbold JF, Sumida Y, Okajima A, Schattenberg JM, Labenz C, Kim W, Lee MS, Wiegand J, Karlas T, Yilmaz Y, Aithal GP, Palaniyappan N, Cassinotto C, Aggarwal S, Garg H, Ooi GJ, Nakajima A, Yoneda M, Ziol M, Barget N, Geier A, Tuthill T, Brosnan MJ, Anstee QM, Neubauer S, Harrison SA, Bossuyt PM, Pavlides M, Investigators L. Diagnostic accuracy of non-invasive tests for advanced fibrosis in patients with NAFLD: an individual patient data meta-analysis. Gut. 2022;71(5):1006-19.

14. Siddiqui MS, Yamada G, Vuppalanchi R, Van Natta M, Loomba R, Guy C, Brandman D, Tonascia J, Chalasani N, Neuschwander-Tetri B, Sanyal AJ, Network NCR. Diagnostic Accuracy of Noninvasive Fibrosis Models to Detect Change in Fibrosis Stage. Clin Gastroenterol Hepatol. 2019;17(9):1877-85 e5.

15. Kunjathoor VV, Febbraio M, Podrez EA, Moore KJ, Andersson L, Koehn S, Rhee JS, Silverstein R, Hoff HF, Freeman MW. Scavenger receptors class A-I/II and CD36 are the principal receptors responsible for the uptake of modified low density lipoprotein leading to lipid loading in macrophages. The Journal of biological chemistry. 2002;277(51):49982-8.

16. Bieghs V, Wouters K, van Gorp PJ, Gijbels MJ, de Winther MP, Binder CJ, Lutjohann D, Febbraio M, Moore KJ, van Bilsen M, Hofker MH, Shiri-Sverdlov R. Role of scavenger receptor A and CD36 in diet-induced nonalcoholic steatohepatitis in hyperlipidemic mice. Gastroenterology. 2010;138(7):2477-86, 86 e1-3.

17. Govaere O, Petersen SK, Martinez-Lopez N, Wouters J, Van Haele M, Mancina RM, Jamialahmadi O, Bilkei-Gorzo O, Lassen PB, Darlay R, Peltier J, Palmer JM, Younes R, Tiniakos D, Aithal GP, Allison M, Vacca M, Goransson M, Berlinguer-Palmini R, Clark JE, Drinnan MJ, Yki-Jarvinen H, Dufour JF, Ekstedt M, Francque S, Petta S, Bugianesi E, Schattenberg JM, Day CP, Cordell HJ, Topal B, Clement K, Romeo S, Ratziu V, Roskams T, Daly AK, Anstee QM, Trost M, Hartlova A. Macrophage scavenger receptor 1 mediates lipid-induced inflammation in non-alcoholic fatty liver disease. J Hepatol. 2022;76(5):1001-12.

18. Pei K, Gui T, Kan D, Feng H, Jin Y, Yang Y, Zhang Q, Du Z, Gai Z, Wu J, Li Y. An Overview of Lipid Metabolism and Nonalcoholic Fatty Liver Disease. Biomed Res Int. 2020;2020:4020249.

19. Bocsan IC, Milaciu MV, Pop RM, Vesa SC, Ciumarnean L, Matei DM, Buzoianu AD. Cytokines Genotype-Phenotype Correlation in Nonalcoholic Steatohepatitis. Oxidative medicine and cellular longevity. 2017;2017:4297206.

20. Arrese M, Cabrera D, Kalergis AM, Feldstein AE. Innate Immunity and Inflammation in NAFLD/NASH. Dig Dis Sci. 2016;61(5):1294-303.

21. Endo M, Masaki T, Seike M, Yoshimatsu H. TNF-alpha induces hepatic steatosis in mice by enhancing gene expression of sterol regulatory element binding protein-1c (SREBP-1c). Experimental biology and medicine (Maywood, NJ). 2007;232(5):614-21.

22. Kim MS, Sweeney TR, Shigenaga JK, Chui LG, Moser A, Grunfeld C, Feingold KR. Tumor necrosis factor and interleukin 1 decrease RXRalpha, PPARalpha, PPARgamma, LXRalpha, and the coactivators SRC-1, PGC-1alpha, and PGC-1beta in liver cells. Metabolism: clinical and experimental. 2007;56(2):267-79.

23. Daemen S, Gainullina A, Kalugotla G, He L, Chan MM, Beals JW, Liss KH, Klein S, Feldstein AE, Finck BN, Artyomov MN, Schilling JD. Dynamic Shifts in the Composition of Resident and Recruited Macrophages Influence Tissue Remodeling in NASH. Cell Reports. 2021;34(2):108626.

24. Katsarou A, Moustakas, II, Pyrina I, Lembessis P, Koutsilieris M, Chatzigeorgiou A. Metabolic inflammation as an instigator of fibrosis during non-alcoholic fatty liver disease. World journal of gastroenterology. 2020;26(17):1993-2011.

25. Uchinami H, Seki E, Brenner DA, D'Armiento J. Loss of MMP 13 attenuates murine hepatic injury and fibrosis during cholestasis. Hepatology. 2006;44(2):420-9.

26. Peters LJF, Jans A, Bartneck M, van der Vorst EPC. Immunomodulatory Nanomedicine for the Treatment of Atherosclerosis. J Clin Med [Internet]. 2021 2021/07//; 10(14):[3185 p.].